

**Early evaluation of
the Global Precipitation Measurement (GPM)
Dual-frequency Precipitation Radar (DPR):
The relation of radar sensitivity with the regional
precipitation characteristics**

(全球降水観測計画 (GPM) 二周波レーダー (DPR)
の初期評価：レーダー感度と降水地域特性の関連性)

Koichi TOYOSHIMA

(豊嶋 紘一)

A dissertation for the degree of Doctor of Science
Department of Earth and Environmental Sciences,
Graduate School of Environmental Studies,
Nagoya University

(名古屋大学大学院 環境学研究科
地球環境科学専攻 学位論文 博士 (理学))

January, 2015

Abstract

The Tropical Rainfall Measuring Mission (TRMM) satellite has been in orbit observing vertical precipitation structure in the tropics until October, 2014, and was taken over to the Global Precipitation Measurement (GPM) mission, launched in February 2014. The purpose of this study is to quantify the sensitivity of Dual-frequency Precipitation Radar (DPR) aboard the GPM mission core observatory, with focus on the Ka-band detectability of light rain and snow in comparison with the Ku-band capability. The GPM is a joint mission by NASA and JAXA for creating the 3-hourly global precipitation map with constellation satellites. In this study, storm top height (STH) is utilized exclusively as the metric of radar sensitivity. The GPM DPR standard product level 2 version 3 is used in this analysis for the period from April to August 2014. Firstly, the global analysis is examined. The radar sensitivity is almost same or better in performance as suggested by the pre-launch test. The Ka high sensitivity (HS) mode and Ku have little systematic difference in STH over a broad range of the histogram, implying that the advantage of the Ka HS mode may not be as distinct as expected. The non-Rayleigh scattering effect may have partly offset the sensitivity advantage of the Ka HS over the Ku. The absence of apparent sensitivity advantage of the Ka high-sensitivity (HS) mode in global statistics is studied in further

depth by investigating the regional characteristics of storm top height (STH). The Ka HS STH generally exceeds the Ku STH across the most of global oceans, owing to the fact that the Ka HS better detects shallow precipitation with STHs around 1 km than the Ku. To further confirm this result, precipitation events detected only by the Ka HS are selected. The enhanced Ka sensitivity is relatively evident, with 10-20 % of the precipitating clouds being detected only at the Ka band, over subtropical and high-latitude oceans where shallow precipitation climatologically prevails. On the other hand, the sensitivity superiority of Ka HS is less evident in the Tropical west Pacific and African rain forest, where deep convection dominates shallow precipitation and the Ku radar is able to capture at least 90 % of precipitation detected by Ka HS. The striking regional dependence of Ku and Ka HS as discussed in this work could be a useful guidance for future climatological applications of DPR.

contents

Chapter 1 Introduction.....	1
1-1 Background.....	1
1-2 Aim of this study	7
Chapter 2 Data and Methodology	8
2-1 Satellite data	8
2-2 Reanalysis data	9
2-3 Definition of storm top height (STH).....	9
Chapter 3 Global analysis of Ku- and Ka- band radar sensitivity.....	11
Chapter 4 Regional Analysis	16
4-1 Analysis Domain	16
4-2 Results	17
Chapter 5 Discussion and Conclusion.....	19
Acknowledgements	24
References	25
Figure Captions	30

Chapter 1 Introduction

1-1 Background

The Global Precipitation Measurement is joint mission by JAXA and NASA. The purpose of this mission is creating the global precipitation map every about three hours. The Multiple satellites orbiting the earth at several inclinations are used for this project. (Figure 1-1). One of the objectives of this mission is increasing the observation area includes the 65°N-65°S. The main part of the GPM project is the core observatory that boards the Dual-Frequency Precipitation Radar (DPR) and the GPM Microwave Imager (GMI) (Figure 1-2). The core observatory was launched by H-IIA Rocket in February 2014. The project was built on the Tropical Rainfall Measuring Mission (TRMM) that is continued to provide high quality global rain maps.

TRMM is a joint mission between JAXA and NASA to observe tropical rainfall, which is launched November 1997. TRMM has several sensors such as first space-borne precipitation radar (PR) and TRMM Microwave Imager (TMI), Visible and Infrared Scanner (VIRS), Clouds and the Earth's Radiant Energy Sensor (CERES),

Lightning Imaging Sensor (LIS) (Figure 1-3). The goal of TRMM project is to understand the dynamical and thermo dynamical mechanisms of the global precipitation systems and microphysical theory (Houze 1981). The observation from the space is suitable for providing precipitation of the global map. To accurate observations, the PR played an important role in this project. The PR provides rainfall structures in the vertical cross section and rain type estimation (Awaka et al. 1997; Iguchi et al. 2000).

The PR consists of 128-element phased array radar. The frequency is 13.8 GHz (Ku-band) (Table 1-1). 32 pulses pairs are transmitted for 49 angle bins. The angle-bin interval is 0.71° over the 215-km swath width (Figure 1-1). The vertical resolution is 250 m. The sensitivity is 0.7mm/h (Kummerow et al. 1998). Figure 2 shows the specification of PR. The orbital altitude was changed 350 km to 402.5 km in 2001, the foot printing size changes 5 km from 4.3 km, and swath width becomes about 245 km from 220 km.

The GPM project has established over the TRMM project achievements. One of the purposes of this GPM mission is improving the observation samples. The sampling error is large in the single satellite observation in TRMM. To obtain global precipitation samples more frequently, multiple microwave imager observation data of constellation

satellite are used for creating 3-hourly global mapping. The other purpose of this project is improving the accuracy of precipitation estimation. The DPR has an important role to improve the accuracy of rain map which is created by microwave imager observations. Other purpose of this project is to improving the observation area. The DPR is able to observe snow in high latitudes for the orbital inclination is 65°. TRMM mainly observes in tropical region so that snow is not for an observation target. The DPR consists of Ku- and Ka-Band radar for precise rainfall measurements.

The average backscattered power is proportional to the Radar Reflectivity Factor (RRF). If the scatterer is smaller than the wavelength, it is called the Rayleigh scattering region where a mean power is effective for in 6 moment of the particle size. The average reflectance is below.

$$\eta = \int_{vol} \sigma_b(D)N(D)dD = \frac{\pi^5}{\lambda^4} |K|^2 \int_0^{D_{max}} D^6 N(D)dD \quad (1-1)$$

Where σ_b is backscattering cross section, K is absorptance of water, D is diameter of droplet, $N(D)$ is droplet size distribution. From this equation, the reflectance is proportional to $1/\lambda^4$. Considering the wavelength of Ka-band is smaller than that of

Ku-band, the average reflectance of Ka-band is superior to Ku-band. The radar reflectivity Z is denoted as sum of 6 moment of the particle size (Fukao et al. 2014; Arai and Liang 2010).

$$Z = \int_0^{D_{max}} D^6 N(D) dD \quad (1-2)$$

The system is upgraded based on the successfully performance of the TRMM with increased sensitivity for snow and light rain in higher latitudes. DPR observation data will be used for rain drop size distribution (DSD). The DPR was developed by JAXA and the National Institute of Information and Communications Technology (NICT) (Figure 1-4). Ku-PR operating at 13.6 GHz and KaPR is 35.55 GHz. Measuring rainfall reflectivity with different band provides rain rate, rain type and vertical structures, and drop size. The KaPR is suitable for snow and light rain detection in high latitudes while the KuPR is suitable for squall-like rain in the tropics.

The radar type is active phased arrays which consisted of 128 transmit and receive modules. The array slotted wave guide antenna has 0.7 degrees beam angle. The angle can be steered 17° on Ku and 8.5° on Ka to the nadir. The swath width is 245 km in KuPR and 120 km in KaPR. KaPR can also operate in a high sensitivity (HS) mode by

interlacing scan that is limited the 120 km swath width. This scan mode provides higher sensitivity measurements of light rain and snow.

The KuPR have 49 angle bins and has 5.2 km footprint at nadir, while Ka Matched scan (MS) mode covers 25 angle bins (Figure 1-5). The matched footprints is utilized for measurements with the dual-frequency algorithm. The accuracy of beam matching is less than 1000 m. The KuPR and KaPR are operated with matching footprints which the same spatial size and scan methodology to collect the data.

In the interlaced high sensitivity scan (HS) mode, the KaPR has 25 angle bins at double pulse widths. To avoid the side lobe clutter contamination, KaPR cannot measure snow and light rain in the out of the swath width region.

The phased array antenna of KuPR is 2.5 m by 2.4 m by 0.6 m size, mass is about 470 kg, the peak power consumption is 446 Watts, and the frequency is 13.597 and 13.603 GHz with a sensitivity of 18 dBZ (Hou et al. 2014) (Table 1-2). The specification of DPR is shown in figure 2. A radar pulse width is 1.67 μ sec (the vertical resolution of 250 m). The maximum transmit power is approximately 1014 W, KuPR is operated at Pulse Repetition Frequencies of 2,900 to 4,500 Hz. While the KaPR radar antenna is 1.2 by 1.44 by 0.7 m size and mass is 336 kg, the peak power is 344 W, the frequency is 35.547 and 35.553 GHz and the sensitivity is 12dBZ (Hou et al.

2014). Depend on the scan mode, the KaPR range resolutions is 250 m (1.67 μ sec pulse width) or 500 m (3.34 μ sec pulse width). The Pulse Repetition Frequencies is 2,900 to 4,500 Hz. The maximum transmit power is about 145 W. Utilizing dual frequencies, wide range of precipitation are able to estimate accurately.

The rainfall retrieval techniques with a DPR have been developed to reduce ambiguity in retrieval of rain rate in comparison with single wavelength radars (Chandrasekar et al. 2003; Rose and Chandrasekar 2005; Liao et al. 2005; Liao and Meneghini 2005; Seto et al. 2013; Kubota et al. 2014). Early observations from the DPR were examined and found to be of great utility for evaluating global cloud resolving models (Kotsuki et al., 2014). The Ka-band detectability of snow and ice particles in comparison with Ku-band is needed to be evaluated.

1-2 Aim of this study

A Ku-band radar has been demonstrated by the TRMM PR to be suitable for measuring moderate to heavy rains typical of the tropical and mid-latitude regions, while a Ka-band radar is expected to extend its ability to capture weak rain and snow in higher latitudes as well (Hou et al. 2008, 2014). Several months of observations from the GPM core observatory are now available, allowing an early evaluation of the instruments onboard. The purpose of this study is to quantify the sensitivity of DPR with focus on the Ka-band detectability of light rain and snow in comparison with the Ku-band capability and to understand the sensitivity difference between the Ku- and Ka-band radars.

In this work, the data and methodology are in chapter 2, the storm top height (STH) definition is in chapter 3. The results will be firstly shown for the global Ku- and Ka-radar sensitivity in chapter 4, and for the regional dependence of precipitation in chapter 5. The summary and conclusion are in chapter 6.

Chapter 2 Data and Methodology

2-1 Satellite data

GPM core observatory observes global precipitation between 65°N and 65°S since March 2014. GPM carries two precipitation radars, operating at the Ku-band (35.55 GHz) with a 245-km wide swath and the Ka-band (13.6 GHz) with a 120-km wide swath. The Ku-band radar (Ku) scan mode has 125-m range bins with 49 angle bins. The Ka- band radar has two different scan modes. One is the matched scan (Ka MS) mode which is matched footprint by footprint with the Ku- band radar and has 125-m range bins with 25 angle bins. Another is the high-sensitivity (Ka HS) mode which has a degraded vertical resolution from 125 m to 250 m to reduce the noise. The Ka HS has footprints interlaced with Ku footprints and has 24 angle bins. The DPR level 2 standard product version 3 provided by JAXA Earth Observation Research Center (EORC) is used in this analysis for the period from April to August 2014.

2-2 Reanalysis data

The Japanese 55-year Reanalysis (JRA55) (Kobayashi et al. 2015) surface air temperature at 2 m is used to isolate out the condition that precipitation is considered to be entirely freezing.

2-3 Definition of storm top height (STH)

STH in the DPR standard product is defined as the altitude of the highest range bin that contains precipitating echoes, where radar reflectivity is required to exceed a given threshold for 6 successive range bins to filter out noise (Figure 2-1). Noise analysis for space-borne radars was given, for example, by Kumagai (1997) and Takahashi and Iguchi (2008). The DPR minimum detectable echo as measured in the pre-launch test is 14.5 dBZ, 16.47 dBZ, and 10.2 dBZ for Ku, Ka MS, and Ka HS, respectively (Kubota, in private communication). These values are better than the nominal sensitivities or 18 dBZ for Ku and 12 dBZ for Ka HS (Hou et al. 2014). These values, however, are not guaranteed to stay valid after the instrument is launched into

orbit. In the DPR product, the radar sensitivity estimated with a signal-to-noise ratio (S/N) threshold is sought for each angle bin based on the noise level determined from echo-free range bins (Kubota, in private communication). This definition of radar sensitivity is robust from an engineering perspective in that it is independent of any arbitrary assumptions except for the additional requirement that 6 continuous bins should all contain echoes above the noise level to define STH. The STH is recalculated in the same manner as done for the DPR product but by varying the threshold every 2 dBZ from 8 dBZ to 20 dBZ in order to ensure the robustness of STH statistics. The analysis is limited to near-nadir (from 21st to 29th) angle bins in order to minimize the influence of the side robe clutters.

Chapter 3 Global analysis of Ku- and Ka- band radar sensitivity

The minimum detectable echoes of Ku and Ka radars generally do not precisely agree with the nominal values determined for the success criterion of the GPM mission. The radar sensitivity could be also slightly changed after launch from the measurements at the pre-launch testing. The minimum detectable echoes in orbit with the actual observations are evaluated and compare them with the nominal and pre-launch values. Figure 3-1 shows the histogram of storm top height calculated with several thresholds with the standard product as the reference for global oceans covered by the GPM core satellite. Some noticeable features are evident in the STH histogram. The Ka MS histogram has a sharp spike at 4-5 km that is absent for Ku, which is ascribed to the inability of Ka MS to detect solid precipitation above the melting layer as described later. Note that a similar peak is observed also for Ka HS with artificially high threshold values but is only barely present for a realistic threshold of 12 dBZ. The Ka MS exhibits a striking dependence on the threshold, showing a long tail toward high altitudes for lowest threshold values, which arises once the threshold decreases to far below the

noise level. A similar histogram tail is also visible for Ka HS when the reflectivity threshold is decreased to 8 dBZ. These results together suggest a guideline for estimating the minimum detectable echo from the STH histogram. First, the threshold would be too low compared to the actual noise level if a histogram tail arises toward the high end. Second, the threshold might be too high if a fictitious melting-layer spike appears, except for Ka MS where the sensitivity is by design so poor that frozen precipitation is largely missed (Figure 3-5). A correct threshold should lie between these two extreme cases. Bearing this in mind, the reflectivity threshold in the standard product (black dotted line in Figure 3-1) that best reproduces the reference STH roughly is hence estimated to be between 12 and 14 dBZ for Ku (3-1a), 18 dBZ for Ka MS (Figure 3-1b) and 12 dBZ for Ka HS (Figure 3-1c). These results suggest that estimated minimum detectable echoes in orbit are roughly consistent with the pre-launch values noted above, although the Ku radar sensitivity is slightly better in orbit.

For Ka HS, the STH histogram appears to entirely lack STHs lower than 1.5 km. This is unrealistic because observational evidence shown later (Figure 3-2) implies a large population of precipitating clouds with STHs below 1.5 km. The failure to detect shallow precipitation arises from the present constraint to define STH. For Ka HS, a high sensitivity is achieved at the expense of a degraded vertical resolution from 125 m

to 250 m, so that contiguous 6 bins inevitably require that STH should be 1.5 km at minimum. In order to avoid this obvious deficiency, the Ka HS STH is recalculated with a series of thresholds defined under 3 successive bins instead of 6 bins. As a result, shallower STHs less than 1.5 km that are undetected in the 6-bin thresholds can be detected for Ka HS and its histogram seems to more naturally capture low-topped precipitation (Figure 3-1d). In the remainder of the paper, STH detection of Ka HS is defined as three successive bins with the 12 dBZ threshold while the reference STH is adopted as it is for Ku and Ka MS.

Figure 3-2 shows the height-latitude histogram of STH in order to demonstrate the STH statistics in the context of global precipitation climatology. The overall distribution is similar across all the radar products, although Ka MS somewhat underestimates the occurrence frequency of high echo tops compared to Ku and Ka HS as expected from Figure 3-1. The higher frequencies around 5 km in Figure 3-2b and 2e is expected by Figure 3-1b which has a spike around freezing height. The STH frequency is concentrated below 2 km for latitudes higher than 60° for the both hemispheres, where moderate precipitation from snow and light rain is typical (Behrangi et al. 2014). Over tropical oceans (30°S-30°N, figure 3-2a, b and c), dual peaks corresponding to shallow cumuli at 2 km and deeper clouds at 5 km height are

seen while the shallow peak is missing over land. This result is consistent with the TRMM PR study by Short and Nakamura (2000). Subtropical oceans (15° - 30°), more notably in the southern hemisphere than in the northern hemisphere, only exhibit a shallow peak as one might expect for regions capped with the trade inversion.

Figure 3-3 shows the STH histogram for three different meridional zones of the tropics (30° S- 30° N), northern extratropics (30° N- 65° N), and southern extratropics (65° S- 30° S) with oceans and lands separated for each zone. The Ka MS histogram exhibits a notable difference from the other two, where the Ka MS mode tends to miss high echo tops (4-7 km for Figure 3-3a and d, 7-12 km for b and e, 4.5-7 km for c and f) and is as a result biased toward low echo tops. The Ka MS fails to detect solid precipitation echoes above the freezing height more frequently than Ku and Ka HS, while generally sensitive to the melting layer (Okamoto et al. 2004). As a result, in the tropics (Figure 3-3b and e) the Ka MS histogram has a striking spike at 4-5 km, because STH settles down on the melting layer whenever ice particles aloft remain undetected. On the other hand, the Ka HS and Ku histograms stay closely together, implying that the sensitivity advantage of the Ka HS mode may not be as distinct as expected. A closer inspection, however, reveals that the Ka HS better captures shallowest echo tops below 1.5 km than the Ku as highlighted by green and red shades in Figure 3-3. Such

precipitation with low STHs typically produces light rain with small raindrops and drizzles or light snow with fluffy snowflakes, which are generally difficult to capture at low microwave frequencies. Moreover, one might argue that the Ka HS is also superior in the ability to measure solid precipitation at 11km or higher in deep convection over tropical continents (Figure 3-3e), whereas there is no such evidence outside the tropics. Overall, the histograms suggest faint hints of the Ka superiority to the Ku in terms of sensitivity, although the differences are minor. The Ka HS sensitivity advantage was also pointed out by Kotsuki et al. (2014).

Figure 3-3 contains both liquid and solid precipitation, but the radar detectability depends on the phase of hydrometeors. To separate rain from snow, Figure 3-4 shows the STH histogram with snowfall isolated out, defined where surface air temperature at 2 m is below 0 °C. The tropical latitudes never meet this criterion and are not shown. The histograms become somewhat sharpened around low STHs, i.e., snow tend to have lower STHs than rain, but are otherwise similar to the previous figures. It follows that the Ka sensitivity to snow may slightly outperform the Ku although the advantage is small.

Chapter 4 Regional Analysis

4-1 Analysis Domain

The analysis domains are defined as shown in Figure 4-1. These selected domains are aimed at extracting different precipitation systems characteristic of each region. Deep convection is often active over the warm pool in Tropical west Pacific (120°E to 150°E, 0° to 15°N), while subtropical shallow cumuli are more dominant in Central Pacific (150°E to 180°, 15°N to 25°N) and stratocumuli prevail in Northeast Pacific (200°E to 240°E, 15°N to 30°N). and Southeast Pacific (240°E to 260°E, 10°S to 20°S), African rain forest (15°E to 35°E, 10°S to 15°N) is selected as an area typical of continental deep convection, while Tibetan Plateau (80°E to 95°E, 30°N to 35°N) is a unique region representing the climate specific to high altitudes. North and South high latitude oceans (0° to 360°, 60°N(S) to 65°N(S)) are chosen as areas dominated by polar precipitation such as rain and snow from relatively low clouds.

4-2 Results

Figure 4-1 shows the global distribution of STH and its pixel count for Ku and Ka HS. The pixel count is the number of the radar footprints with STH detected throughout the analysis periods over a $0.5^\circ \times 0.5^\circ$ grid. The STH distribution of KaHS closely resembles that of Ku, but a closer examination reveals some differences. Subtropical oceans off the western coasts of a continent are blanked out for Ku while mostly filled for Ka HS, implying the presence of the clouds only detectable by Ka HS in these regions, known to be covered with stratocumuli rarely producing heavy rain. Figure 4-1c shows the STH difference between Ku and Ka HS. The Ka HS STH generally exceeds the Ku STH across the global oceans with the possible exception of intertropical convergence zones (ITCZs). Ku tends to be higher in STH than Ka HS over continents. Difference in the pixel count (Figure 4-1f) indicates that Ka HS detects more precipitation than Ku widely over the globe except for subtropical oceans immediately outside the ITCZs. Figure 4-2 and 4-3 show the STH histograms for selected regions. In the Northwest Pacific (Figure 4-2a), the congestus peak is seen around 3 km and signals from within and above the melting layer are detected by both radars, exemplifying the typical members of tropical convection (Johnson et al. 1999).

There are minor differences near 1 km and higher altitudes than the freezing level, although it is unclear at this point whether the differences are statistically robust. In the central north Pacific, the congestus peak around 3 km is somewhat more conspicuous for Ku than Ka HS, which might be responsible of the marginally higher detectability of Ku than Ka HS in this region (Figure 4-2b). A shallower STH around 1-1.5 km dominates the Northeast (Figure 4-2c) and Southeast Pacific (Figure 4-2d). This shallow peak is sharper and is located at a slightly lower STH for Ka HS than Ku. The African rain forest (Figure 4-3a) is reminiscent of the Northwest Pacific except for the lack of a congestus peak, which is known to be absent over land (Short and Nakamura, 2000). As for the Tibetan plateau (Figure 4-3b), the STH peaks around 8 km, similarly to the ground radar measurements by Uyeda et al. (2001), and the Ku and Ka HS histograms are similar over the whole range of STH. The STH is sharply peaked around 1 km and its tail tapers off below 7 km in the southern high latitudes (Figure 4-3d) and below 5 km in the northern high latitudes (Figure 4-3c). Ka HS more clearly captures the 1-km peak in these regions, similarly to the Northeast and Southeast Pacific.

Chapter 5 Discussion and Conclusion

This analysis aimed at an early evaluation of the GPM DPR performance with focus on exploring the expected difference in precipitation detectability between the Ku- and Ka-band radars. My interest is to understand to what extent the Ka-band radar is able to detect weak rain and solid state precipitation compared to Ku-band radar. The detectability of the Ku-band radar and two modes of the Ka-band radar (Ka MS and Ka HS) is studied in terms of STH. STH for the Ka HS is redefined with a modified criterion so as to avoid the underrepresentation of shallow precipitation that was found in the original definition. While the Ka MS is found to be least sensitive to high echo tops, the sensitivity advantage of the Ka HS over the Ku is not very evident. A close examination suggests that the Ka HS may be slightly better at capturing weak rain and snow, although the differences are minor. The difference in sensitivity among different radar frequencies has been studied previously in various contexts. Berg et al. (2009) investigated the precipitation detectability of the TRMM PR and CloudSat W-band radar in attempt to construct the histogram over a full range of precipitation rate beyond the capability of individual instruments. The possibility to separate the liquid and ice phases of precipitation was explored by utilizing the sensitivity difference between the

Ku and Ka bands (Liao and Meneghini, 2011).

The absence of apparent superiority of the Ka-band radar in terms of precipitation detectability is in part owing to the non-Rayleigh scattering effect. While the Rayleigh approximation marginally holds at the Ku band with the exception of heaviest rain events, it is no longer valid at the Ka band for a broad range of rain rate (L'Ecuyer and Stephens 2002). This difference in the degree to which the Rayleigh approximation is violated would introduce a frequency dependence in radar reflectivity expressed in dBZ (e.g., Matrosov, 1992), generally leading to smaller values at the Ka band than at the Ku. The effect should partly offset the sensitivity advantage of the Ka HS over the Ku, and probably accounts for the current finding that the Ka HS seems not to considerably exceed the Ku in the ability to detect light rain and snow.

Another possible factor to take into account is that the actual Ku-band radar detectability turned out to outperform the original instrumental design and effectively offset the superiority of Ka HS to some extent. The minimum detectable echo of the Ku-band radar was nominally 18 dBZ (Hou et al. 2014), while it was as good as 14.5 dBZ in the pre-launch test. It should be also noted that this current analysis period is limited to 5 months of boreal spring summer. Snow and light rain in the northern hemisphere winter are not included and could potentially affect the representativeness

of the present statistics.

The Regional difference of precipitation of regional dependency is examined. Figure 4-2 and 4-3 show that the STH histogram for each selected region exhibits consistent features common to Ku and Ka HS (Toyoshima et al. 2015). Also found, however, is a hint of evidence that Ku and Ka HS may differ in sensitivity for specific types of precipitating clouds because the difference in STH histogram, although subtle, emerges in systematically different ways among the regions. To make sure that this subtle difference is a real signal, another analysis is performed with an additional screening applied to Ka HS footprints so as to isolate out the precipitating clouds detectable only by Ka HS. Since Ku and Ka HS footprints are interlaced with each other, precipitating Ka HS footprint, defined by the presence of 3 contiguous range bins with echoes above the threshold, is further constrained by the surrounding 4 Ku footprints that are required to be all precipitation free (Figure 4-4). The dotted lines in Figure 4-3 and 4 show the STH histogram for precipitation detected only by Ka HS (hereafter the Ka-only precipitation). By definition, the total pixel count is significantly smaller than the unconstrained Ka HS histogram. For most regions, the Ka-only precipitation accounts partly for shallow precipitation with a STH around 1-1.5 km. This supports the above finding that Ka HS outperforms Ku in the detectability of shallow precipitation to

some degree. A better sensitivity to shallow precipitation is probably a primary reason why Ka HS STH is generally lower than Ku STH (Figure 4-1c). On the other hand, Ka HS is presumably somewhat better in the ability to detect ice particles aloft in deep convection as implied by enhanced histogram tails toward high STHs in the Tropical west Pacific and African rain forest, or the regions where Ka HS has higher STHs than Ku. A melting layer peak is also visible in the Ka-only histogram for the Tropical west Pacific and African rain forest, which might suggest a very weak stratiform precipitation. The Tibetan Plateau shows a broad Ka-only histogram, which is a feature not observed in any other regions currently studied.

Table 1 shows the pixel count ratio of Ku-detected precipitation and Ka-only precipitation each relative to all Ka-detected precipitation. More than 10 % of precipitation detected by Ka HS does not accompany Ku-band echoes in the regions typical of shallow precipitation such as the Northeast and Southeast Pacific as well as high latitudes. Ku detects about 70-80 % of precipitation that is identified by Ka HS in those regions. In contrast, the sensitivity superiority of Ka HS is less evident in the Tropical west Pacific and African rain forest, where deep convection dominates shallow precipitation. The sensitivity advantage of Ka HS almost vanishes in these regions, where Ku is able to capture at least 90 % of precipitation detected by Ka HS.

Figure 4-5 shows that schematic image of summary. KaHS has higher sensitivity for the shallower precipitation than Ku. The STH climatological map shows lower STH in this regime. While much of deep convection in Tropical west Pacific and African rain forest, Ka HS is presumably somewhat better in the ability to detect ice particles aloft in deep convection. The STH difference climatological map shows higher (blue region) STH difference in this regime.

The Tibetan Plateau and Central Pacific exhibit some unique features in STH statistics that are not fully understood at this point. The striking regional dependence of Ku and Ka HS as discussed in this work could be a useful guidance for future climatological applications of DPR.

Acknowledgements

The author would like to thank to my advisor Prof. H. Masunaga for encouraging my research. His advices on research have been invaluable. The author also would like to appreciate Dr. F. A. Furuzawa for discussions. I wish to thank Prof. H. Uyeda and Prof. K. Tsuboki for his constructive comments and discussions. The author also would like to thank our group members and Ms. T. Tanaka for vigorous assistance and Dr. H. Minda for supporting computer server systems. The author also would like to thank Prof. K. Nakamura (Univ. Dokkyo) and M. Hirose (Univ. Meijo) for valuable comment and discussions. The author also would like to thank Dr. T. Kubaota (JAXA) and H. Hanado (NICT) and J. Awaka (Univ. Tokai) for valuable comment about GPM product algorithm. The author also has special thanks to my family. All of you have been there to support me for my Ph.D. thesis.

The GPM data used in this study were provided by JAXA. The author also would like to appreciate JAXA/EORC and GPM project. The reanalysis datasets used for this study are provided from the JRA-55 project carried out by the Japan Meteorological Agency (JMA).

References

- Arai, K., X. Liang, 2010: A comparative study between Mie and Rayleigh scattering assumption based estimation of Z-R relation and rainfall rate with TRMM/PR data. *Japan Society of photogrammetry and Remote Sensing*, **27**(49), 67-74.
- Awaka, J., T. Iguchi, H. Kumagai and K. Okamoto, 1997: Rain type classification algorithm for TRMM precipitation radar. *Proc. IGARSS '97*, Singapore, IEEE, 1633-1635.
- Behrangi, A., G. Stephens, R. F. Adler, G. J. Huffman, B. Lambriksen, and M. Lebsock, 2014: An update on oceanic precipitation rate and its zonal distribution in light of advanced observations from space. *J Climate*, **27**(11), 3957-3965.
- Berg, W., T. L'Ecuyer, and J. M. Haynes, 2010: The distribution of rainfall over oceans from spaceborne radars. *J. Appl. Meteor. Climatol.*, **49**(3), 535–543.
- Chandrasekar, V., H. Fukatsu, and K. Mubarak, 2003: Global mapping of attenuation at Ku-and Ka-band. *IEEE Trans. Geosci. Remote Sens.*, **41**(10), 2166-2176.
- Fukao, S., K. Hamazu and, R. J. Doviak, 2014: *Radar for Meteorological and Atmospheric Observations*, Springer, 537 pp.

Hou, A. Y., G. Skofronick-Jackson, C. D. Kummerow, and J. M. Shepherd, 2008:

Global precipitation measurement: Advances in measurement, estimation and prediction, Springer Berlin Heidelberg, 131-169.

Hou, A. Y., R. K. Kakar, S. Neeck, A. A. Azarbarzin, C. D. Kummerow, M. Kojima, R.

Oki, K. Nakamura, and T. Iguchi, 2014: The Global Precipitation Measurement (GPM) mission., *Bull. Amer. Meteor. Soc.*, **95**(5), 701–722.

Iguchi, T., T. Kozu, R. Meneghini, J. Awaka, K. Okamoto, 2000: Rain-profiling

algorithm for the TRMM precipitation radar. *J. Appl. Meteor.*, **39**, 2038-2052.

Johnson H. R., T. M. Rickenbach, S. A. Rutledge, P. E. Ciesielski, and W. H. Schubert,

1999: Trimodal Characteristics of Tropical Convection. *J. Climate*, **12**, 2397–2418.

Kobayashi, S., Y. Ota, Y. Harada, A. Ebata, M. Moriya, H. Onoda, K. Onogi, H.

Kamahori, C. Kobayashi, H. Endo, K. Miyaoka, and K. Takahashi, 2015: The JRA-55 Reanalysis: General Specifications and Basic Characteristics. *J. Meteor. Soc. Japan.*, **93**. doi:10.2151/jmsj.2015-001.

Kotsuki, S., K. Terasaki, and T. Miyoshi, 2014: GPM/DPR Precipitation Compared with

a 3.5-km-Resolution NICAM Simulation. *SOLA*, **10**, 204-209.

Kubota, T., N. Yoshida, S. Urita, T. Iguchi, S. Seto, R. Meneghini, J. Awaka, H. Hanado,

S. Kida, and R. Oki, 2014: Evaluation of Precipitation Estimates by at-Launch

- Codes of GPM/DPR Algorithms Using Synthetic Data from TRMM/PR Observations. *IEEE J-STARS.*, 1-15.
- Kumagai, H., T. Kozu, and T. Iguchi, 1997: Rain/no-rain discrimination for TRMM precipitation radar. *IEEE Trans. Geosci. Remote Sens.*, **3**, 1111-1113.
- Kummerow, C., J. Simpson, O. Thiele, W. Barnes, A. T. C. Chang, E. Stocker, R. F. Adler, A. Hou, R. Kakar, F. Wentz, P. Ashcroft, T. Kozu, Y. Hong, K. Okamoto, T. Iguchi, H. Kuroiwa, E. Im, Z. Haddad, G. Huffman, B. Ferrier, W. S. Olson, E. Zipser, E. A. Smith, T. T. Wilheit, G. North, T. Krishnamurti, and K. Nakamura, 2000: The Status of the Tropical Rainfall Measuring Mission (TRMM) after Two Years in Orbit. *J. Appl. Meteor.*, **39**, 1965-1982
- L'Ecuyer, T. S., and G. L. Stephens, 2002: An estimation-based precipitation retrieval algorithm for attenuating radars. *J. Appl. Meteor.*, **41**(3), 272–285.
- Liao, L., R. Meneghini, T. Iguchi, and A. Detwiler, 2005: Use of dual-wavelength radar for snow parameter estimates. *J. Atmos. Oceanic Technol.*, **22**(10), 1494-1506.
- Liao, L., and R. Meneghini, 2005: A study of air/space-borne dual-wavelength radar for estimation of rain profiles. *Adv. Atmos. Sci.*, **22**(6), 841-851.
- Liao L. and R. Meneghini, 2011: A Study on the Feasibility of Dual-Wavelength Radar for Identification of Hydrometeor Phases. *J. Appl. Meteor. Climatol.*, **50**(2),

449-456.

Matrosov, S. Y., 1992: Radar reflectivity in snowfall. *IEEE Trans. Geosci. Remote Sens.*, **30**, 454-461.

Okamoto, K., H. Sasaki, E. Deguchi, and M. Thurai, 2004: Bright-Band Height Statistics Observed by the TRMM Precipitation Radar. The 2nd TRMM International Science Conference, Nara. 9.

Rose, C. R., and V. Chandrasekar, 2005: A systems approach to GPM dual-frequency retrieval. *IEEE Trans. Geosci. Remote Sens.*, **43**(8), 1816-1826.

Seto, S., T. Iguchi, and T. Oki, 2013: The Basic Performance of a Precipitation Retrieval Algorithm for the Global Precipitation Measurement Mission's Single/Dual-Frequency Radar Measurements. *IEEE Trans. Geosci. Remote Sens.*, **51**(12), 5239-5251.

Short, D. A., and K. Nakamura, 2000: TRMM radar observations of shallow precipitation over the tropical oceans. *J. Climate*, **13**, 4107-4124.

Takahashi, N., and Iguchi, T., 2008: Characteristics of TRMM/PR system noise and their application to the rain detection algorithm. *IEEE Trans. Geosci. Remote Sens.*, **46**(6), 1697-1704.

Toyoshima, K., H. Masunaga, and F. A. Furuzawa, 2015: Early evaluation of Ku- and

Ka-band sensitivities for the Global Precipitation Measurement (GPM)

Dual-frequency Precipitation Radar (DPR). *SOLA*, **11**, 13-16.

Uyeda, H., H. Yamada, J. Horikomi, R. Shirooka, S. Shimizu, L. Liping, K. Ueno, H.

Fujii and T. Koike, 2001: Characteristics of convective clouds observed by a Doppler

radar at Naqu on Tibetan Plateau during the GAME-Tibet IOP. *J. Meteor. Soc. Japan*,

79, 463-474.

Figure Captions

Fig. 1-1. GPM constellation satellites. Multiple satellites data are used for 3-hourly global map. *(provided by NASA)*

Fig. 1-2. GPM core observatory. The dual-frequency radar and microwave imager are mounted on the satellite. *(provided by NASA)*

Fig. 1-3. The TRMM observatory *(provided by JAXA)*. TRMM has several sensors such as first space-borne precipitation radar (PR) and TRMM Microwave Imager (TMI), Visible and Infrared Scanner (VIRS), Clouds and the Earth's Radiant Energy Sensor (CERES), Lightning Imaging Sensor (LIS).

Fig. 1-4. The DPR phased array antenna. Left is Ka-radar, right is Ku-radar. *(provided by JAXA)*

Fig. 1-5. DPR scan modes. Green circle means KuPR foot prints, yellow circle means KaPR matched scan mode and pink circle means KaPR high sensitivity mode. *(provided by JAXA)*

Table 1-1. The specifications of TRMM PR (Kummerow et al. 1998)

Fig. 1-5. DPR scan modes *(provided by JAXA)*

Table 1-2. GPM instruments specifications comparing with TRMM PR. (Hou et al.

2014)

Fig. 2-1. Schematic figure for STH definition in standard product.

Fig. 3-1. The normalized histogram of STH for global oceans within the observational coverage of GPM DPR. The reference STH from the GPM standard product is plotted in black, and STHs recalculated with different reflectivity thresholds of 12, 14, 16, 18, and 20 dBZ are delineated in colors as indicated for Ku (a), Ka MS (b) and Ka HS (c). (d) is same as (c) but with 3 instead of 6 successive ranges bins to define STH.

Fig. 3-2. The height-latitude histogram of STH. The frequency of occurrence is normalized at each latitude. (a) Ku Ocean, (b) Ka MS Ocean, (c) Ka HS Ocean, (d) Ku Land, (e) Ka MS Land, (f) Ka HS Land. The contour lines are drawn at each 0.03 step up to 0.15.

Fig. 3-3. The STH histogram for Ku, Ka MS, and Ka HS for (a) 30°N-65°N ocean, (b) 30°S-30°N ocean, (c) 30°S-65°S ocean, (d) 30°N-65°N land, (e) 30°S-30°N land, (f) 30°S-65°S land. For visual clarity, the difference between Ku and Ka HS is shaded in red where Ku exceeds Ka HS and in green otherwise.

Fig. 3-4. As Figure 2a, c, d and f, but only for the regions where surface air temperature at 2 m is below 0°C. (a) 30°N-65°N ocean, (b) 30°S-65°S ocean, (c) 30°N-65°N

land, (d) 30°S-65°S land.

Fig. 4-1. Global map of STH and pixel counts for Ku (a and d), KaHS (b and e), and Ku minus Ka HS (c and f). The selected regions are indicated by boxes (Tropical west pacific, Central Pacific, Northeast Pacific, Southeast Pacific, African rain forest, Tibetan Plateau, North high latitude, South high latitude).

Fig. 4-2. The STH histograms for the selected regions (a) Tropical west pacific, (b) Central Pacific, (c) Northeast Pacific, (d) Southeast Pacific.

Fig. 4-3. As for Figure 2 but (a) African rain forest, (b) Tibetan Plateau, (c) North high latitude, (d) South high latitude.

Fig. 4-4. Schematic for defining pixels with precipitation detected only by Ka HS.

Fig. 4-5. schematic image of summary. KaHS has higher sensitivity for the shallower precipitation than Ku. The STH climatological map shows lower STH in this regime. While much of deep convection in Tropical west Pacific and African rain forest, Ka HS is presumably somewhat better in the ability to detect ice particles aloft in deep convection. The STH difference climatological map shows higher (blue region) STH difference in this regime.

Table. 4-1. Number fraction of Ku detected precipitation (Ku_{all} , middle column) and precipitation detected only by Ka HS (Ka_{only} , right column) as normalized by Ka HS

detected precipitation ($K_{a_{all}}$) for each selected region.

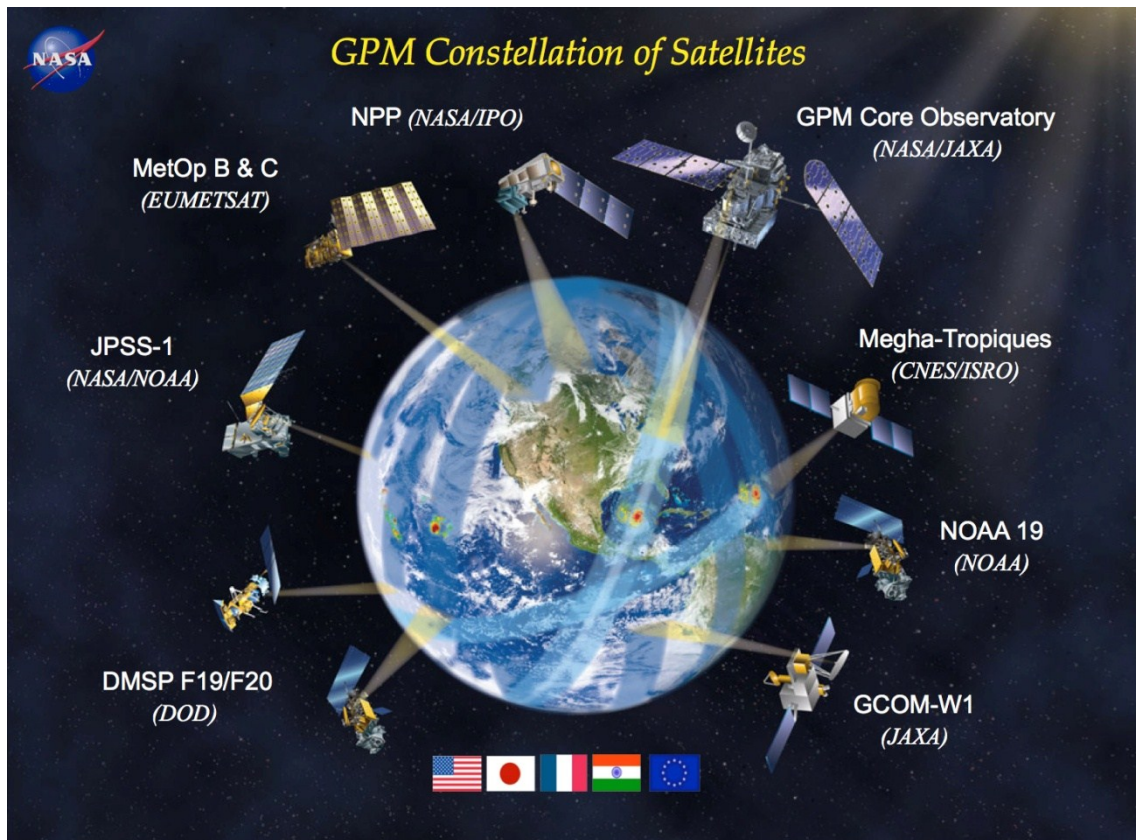


Figure 1-1

GPM constellation satellites. Multiple satellites data are used for 3-hourly global map.

(http://www.nasa.gov/sites/default/files/images/740891main_GPM_constellation_updated_8_25_11.jpg)

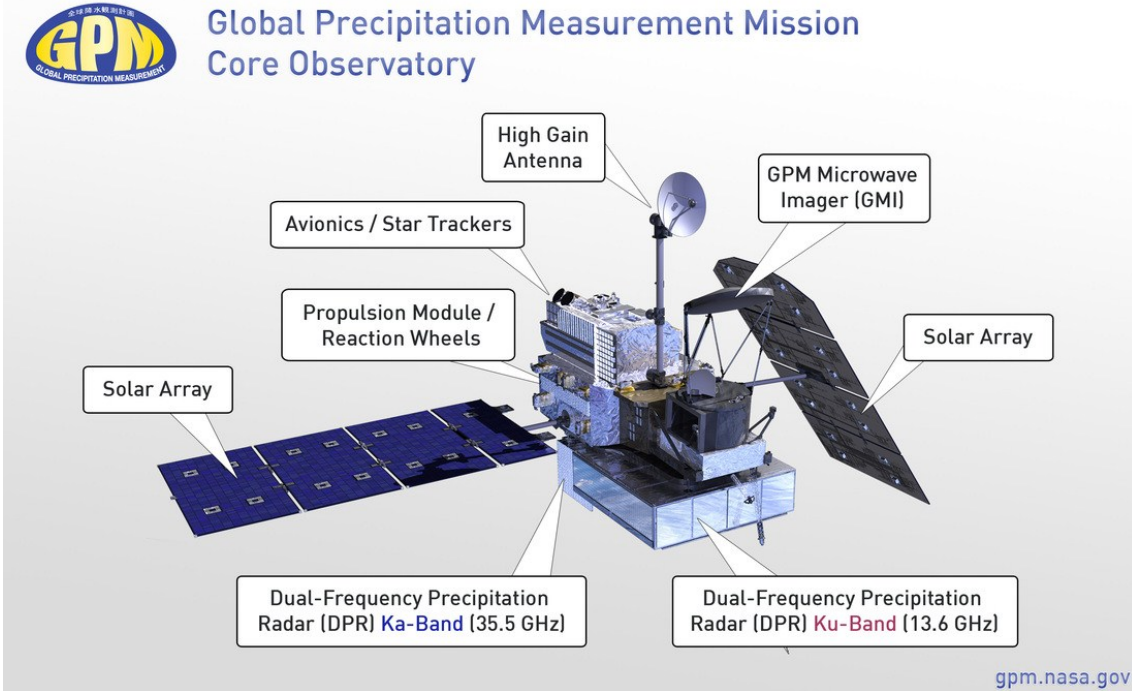


Figure 1-2

GPM core observatory. The dual-frequency radar and microwave imager are mounted on the satellite.

(http://pmm.nasa.gov/sites/default/files/imageGallery/GPM-Core-diagram-extended-FI_NAL2.jpg)

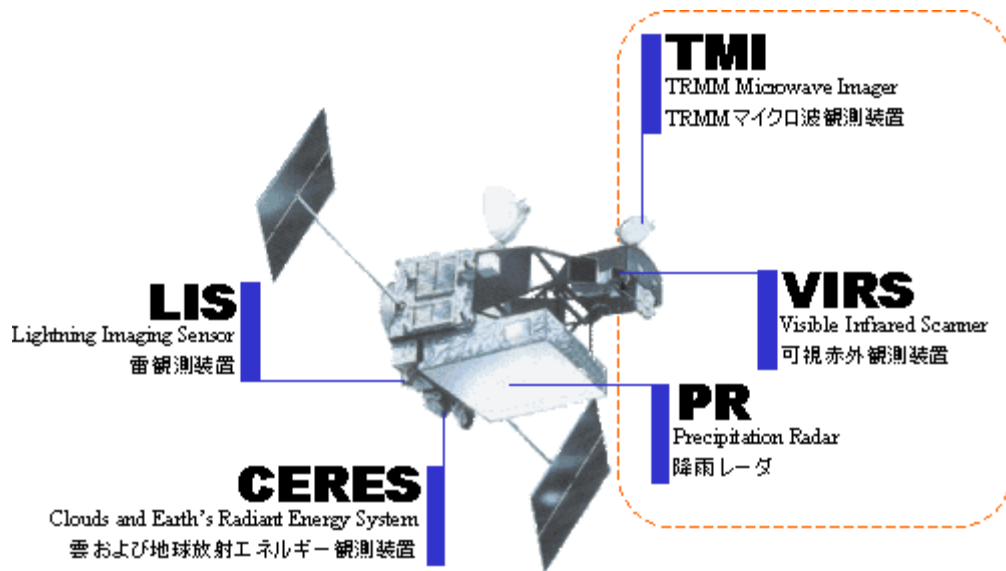


Figure 1-3

The TRMM observatory and instruments. TRMM has several sensors such as first space-borne precipitation radar (PR) and TRMM Microwave Imager (TMI), Visible and Infrared Scanner (VIRS), Clouds and the Earth's Radiant Energy Sensor (CERES), Lightning Imaging Sensor (LIS).

(<http://www.eorc.jaxa.jp/TRMM/document/text4/image/trmm.gif>).

Item	Specification
Frequency	13.796, 13.802 GHz
Sensitivity	$\leq \sim 0.7 \text{ mm h}^{-1}$ (S/N/pulse ≈ 0 dB)
Swath width	215 km
Observable range	Surface to 15-km altitude
Horizontal resolution	4.3 km (nadir)
Vertical resolution	0.25 km (nadir)
Antenna	
Type	128-element WG planar array
Beamwidth	$0.71^\circ \times 0.71^\circ$
Aperture	2.0 m \times 2.0 m
Scan angle	$\pm 17^\circ$ (Cross-track scan)
Transmitter/receiver	
Type	SSPA and LNA (128 channels)
Peak power	$\geq 500 \text{ W}$ (at antenna input)
Pulse width	1.6 $\mu\text{s} \times 2$ ch. (transmitted pulse)
PRF	2776 Hz
Dynamic range	$\geq 70 \text{ dB}$
Number of independent samples	64
Data rate	93.2 kbps

Kummerow et al. 1998

Table 1-1

The specifications of TRMM PR (Kummerow et al. 1998)

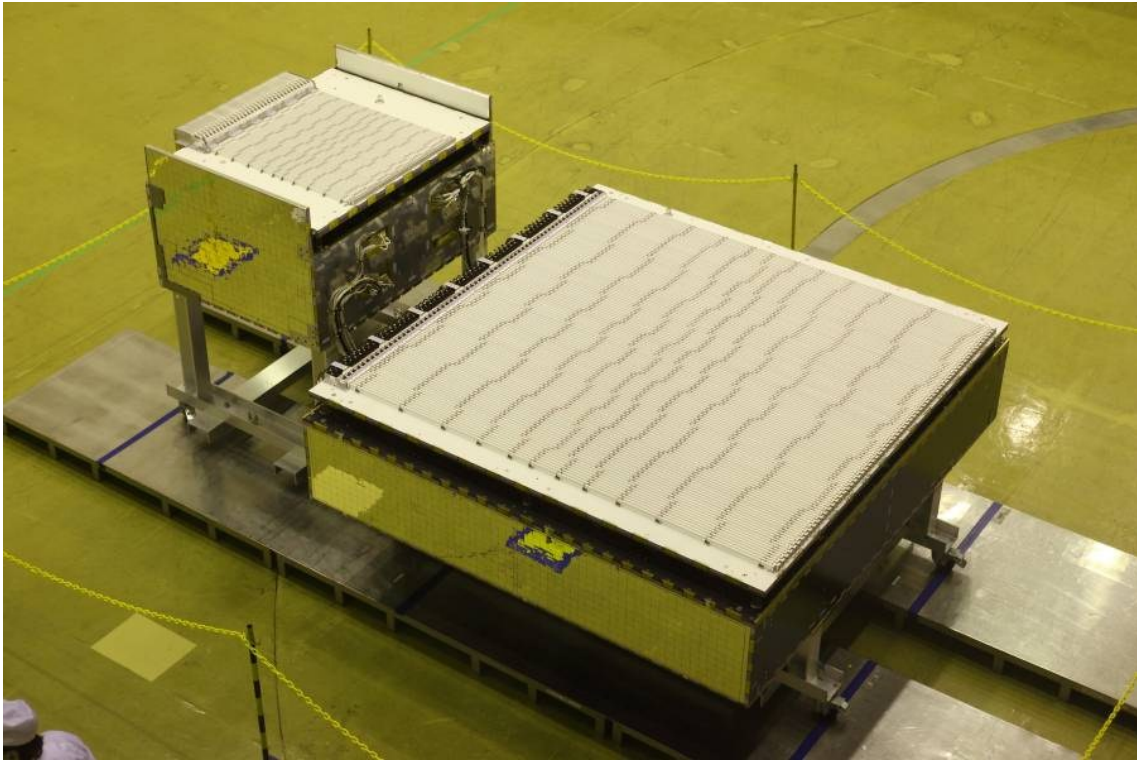


Figure 1-4

The DPR phased array antenna. Left is Ka-radar, right is Ku-radar.

(http://www.satnavi.jaxa.jp/project/gpm/news/2012/img/gpm_03.jpg)

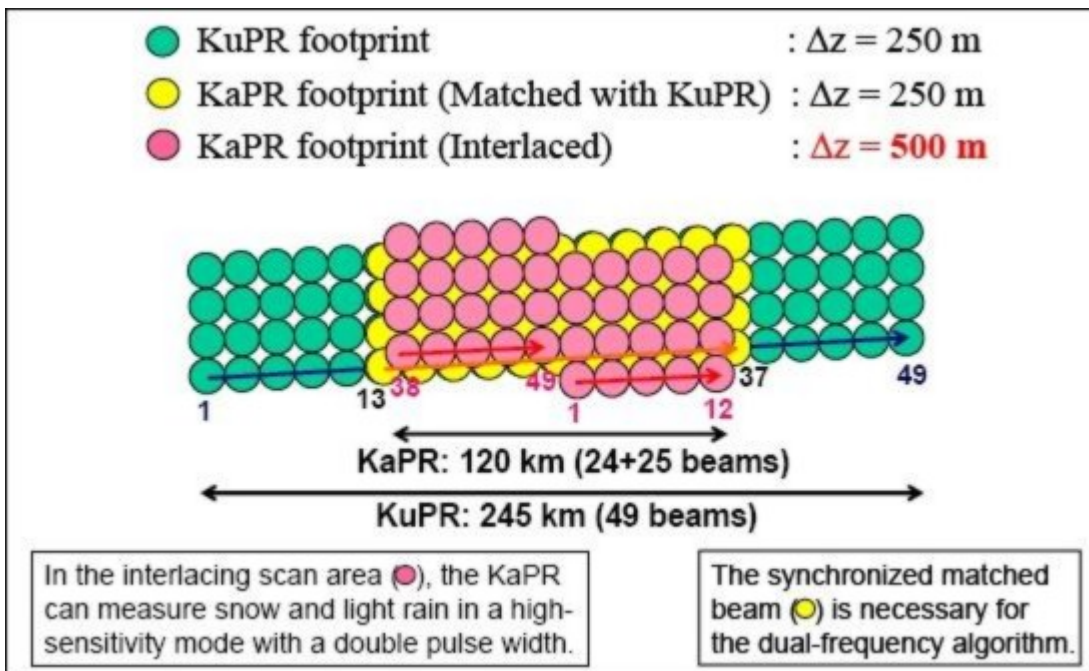


Figure 1-5

DPR scan modes. Green circle means KuPR foot prints, yellow circle means KaPR matched scan mode and pink circle means KaPR high sensitivity mode.

(https://directory.eoportal.org/documents/163813/432525/GPM_Auto13)

TABLE 2. Comparison of GPM DPR instrument characteristics with TRMM PR.			
Instrument	GPM KaPR at 407 km	GPM KuPR at 407 km	TRMM KuPR at 350 km
Antenna type	Active phased array (128)	Active phased array (128)	Active phased array (128)
Frequency (GHz)	35.547 and 35.553	13.597 and 13.603	13.796 and 13.802
Swath width (km)	120	245	215
Horizontal resolution at nadir (km)	5	5	4.3
Transmitter pulse width (μ s)	1.6/3.2 ($\times 2$)	1.6 ($\times 2$)	1.6 ($\times 2$)
Range resolution (m)	250/500	250	250
Observation range (km) (mirror image at nadir)	18 to -3	18 to -5	15 to -5
Pulse repetition frequency (Hz)	Variable (4275 \pm 100)	Variable (4206 \pm 170)	Fixed (2776)
Sampling number	108 ~ 112	104 ~ 112	64
Transmitter peak power (W)	>146	>1013	>500
Minimum detectable Z_e and rain rate*	12 dBZ (500 m res.) (0.2 mm h ⁻¹)	18 dBZ (0.5 mm h ⁻¹)	18 dBZ (0.7 mm h ⁻¹)
Measurement accuracy (dBZ)	< ± 1	< ± 1	< ± 1
Data rate (Kbps)	<78	<112	<93.5
Mass (kg)	<300	<365	<465
Power consumption (W)	<297	<383	<250
Physical dimensions (m)	1.44 \times 1.07 \times 0.7	2.4 \times 2.4 \times 0.6	2.2 \times 2.2 \times 0.6

* Minimum detectable rain rate defined as $Z_e = 200 R^{1.6}$ for DPR and $Z_e = 372.4 R^{1.54}$ for TRMM PR.

Table 1-2

GPM instruments specifications comparing with TRMM PR. (Hou et al. 2014)

Definition of Storm top height (STH) in standard product

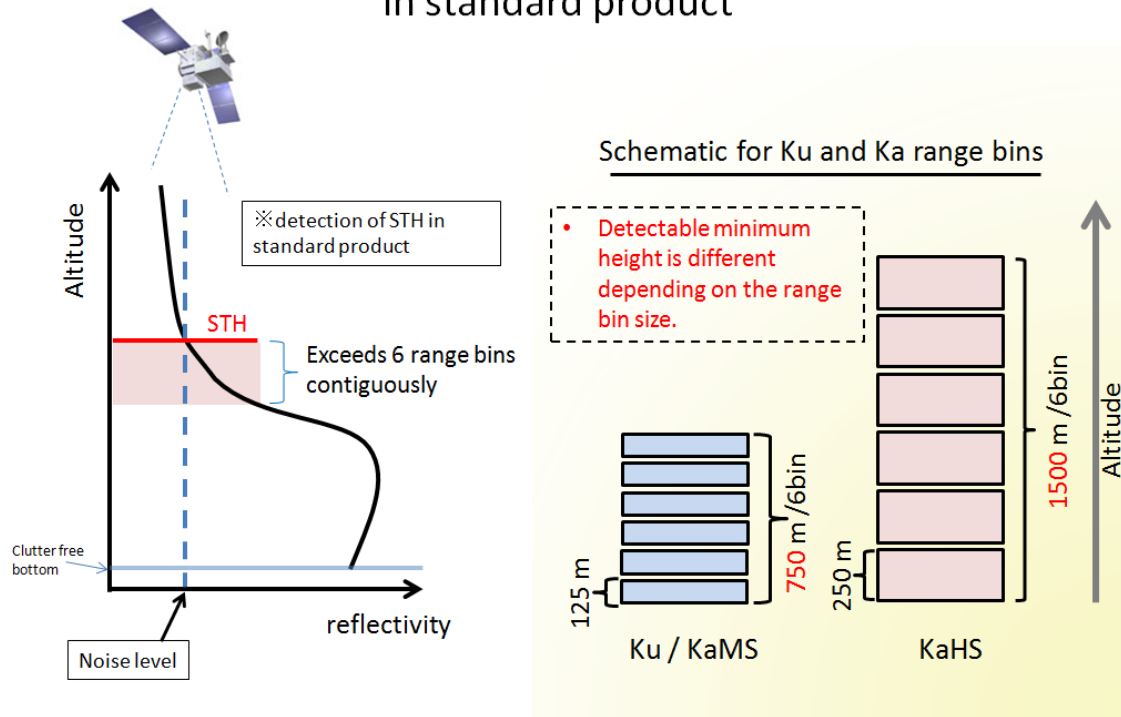


Figure 2-1

Schematic figure for STH definition in standard product.

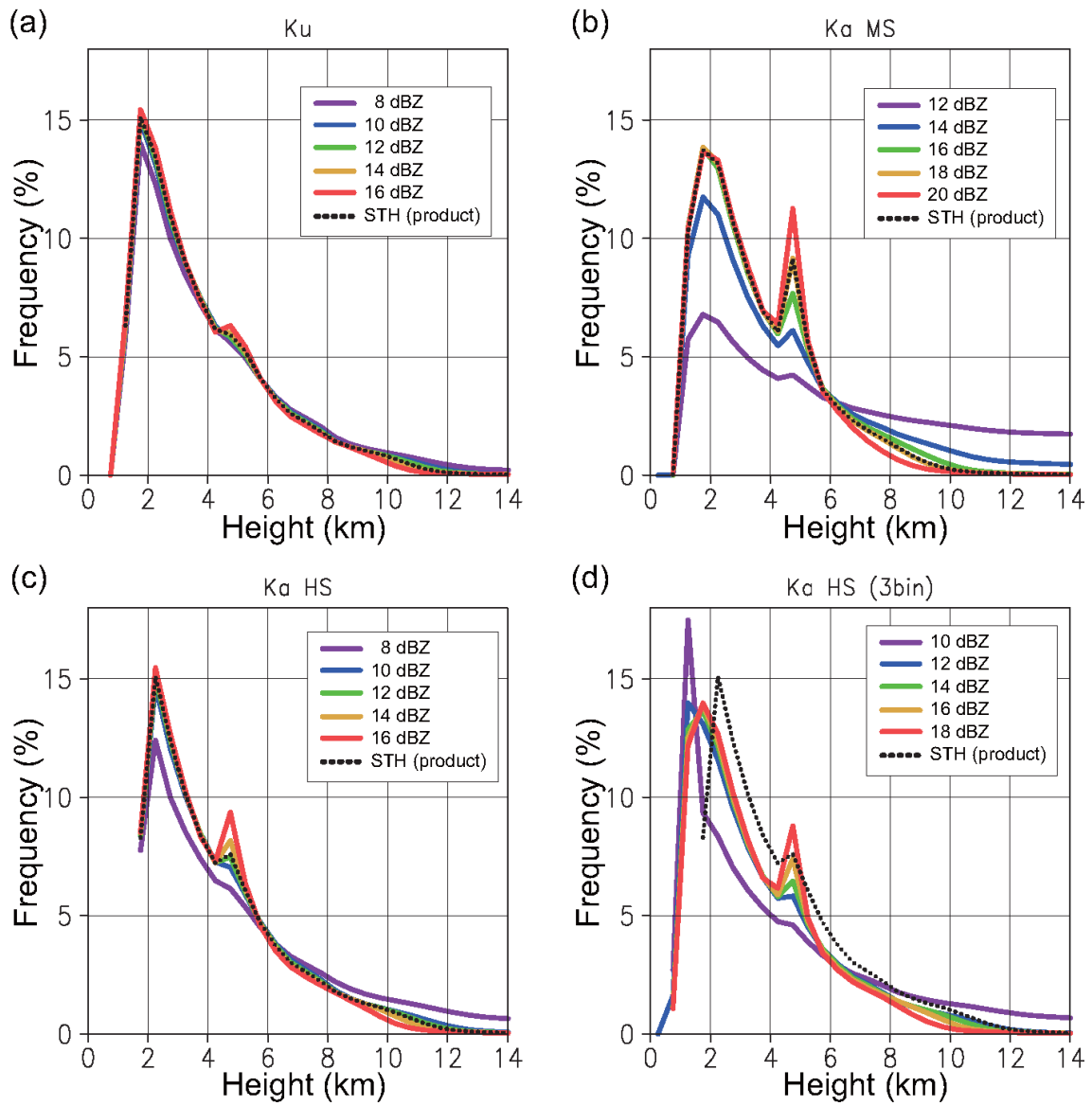


Figure 3-1

The normalized histogram of STH for global oceans within the observational coverage of GPM DPR. The reference STH from the GPM standard product is plotted in black, and STHs recalculated with different reflectivity thresholds of 12, 14, 16, 18, and 20

dBZ are delineated in colors as indicated for Ku (a), Ka MS (b) and Ka HS (c). (d) is same as (c) but with 3 instead of 6 successive ranges bins to define STH.

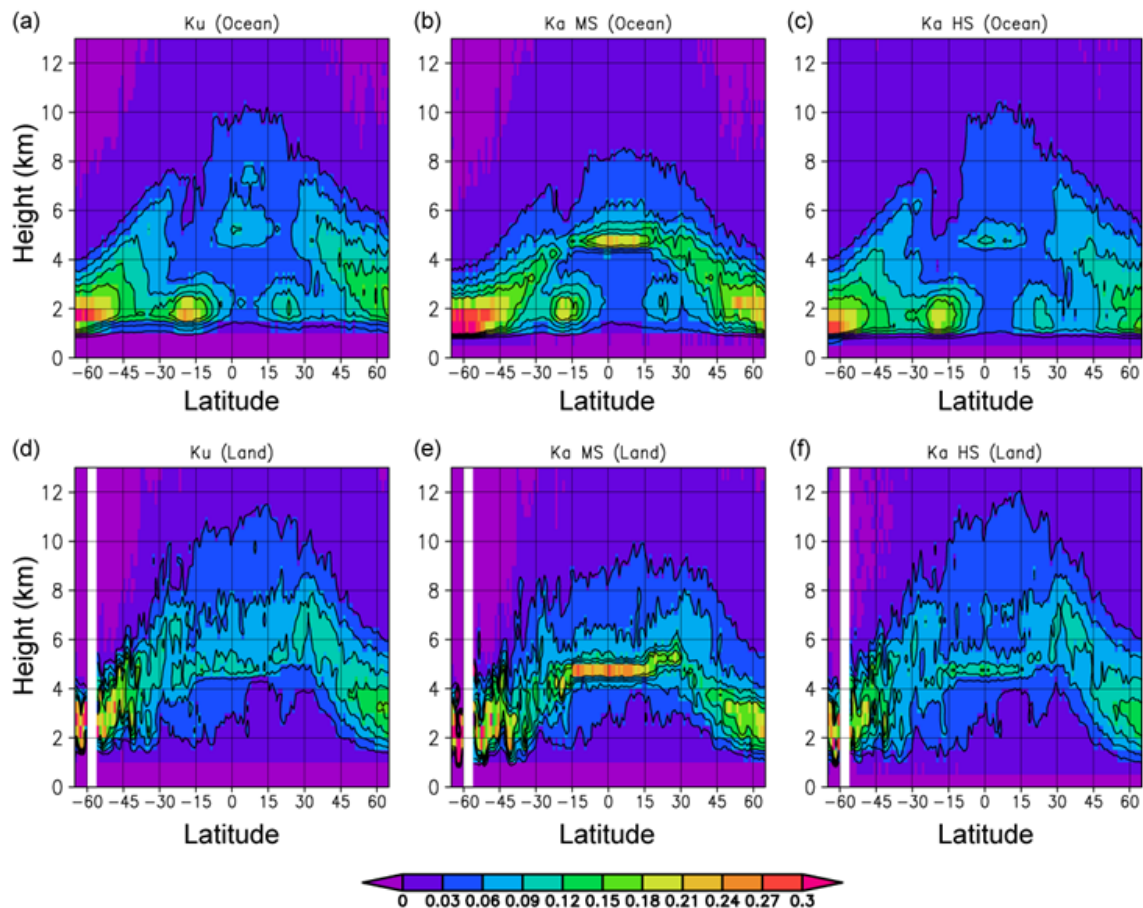


Figure 3-2

The height-latitude histogram of STH. The frequency of occurrence is normalized at each latitude. (a) Ku Ocean, (b) Ka MS Ocean, (c) Ka HS Ocean, (d) Ku Land, (e) Ka MS Land, (f) Ka HS Land. The contour lines are drawn at each 0.03 step up to 0.15.

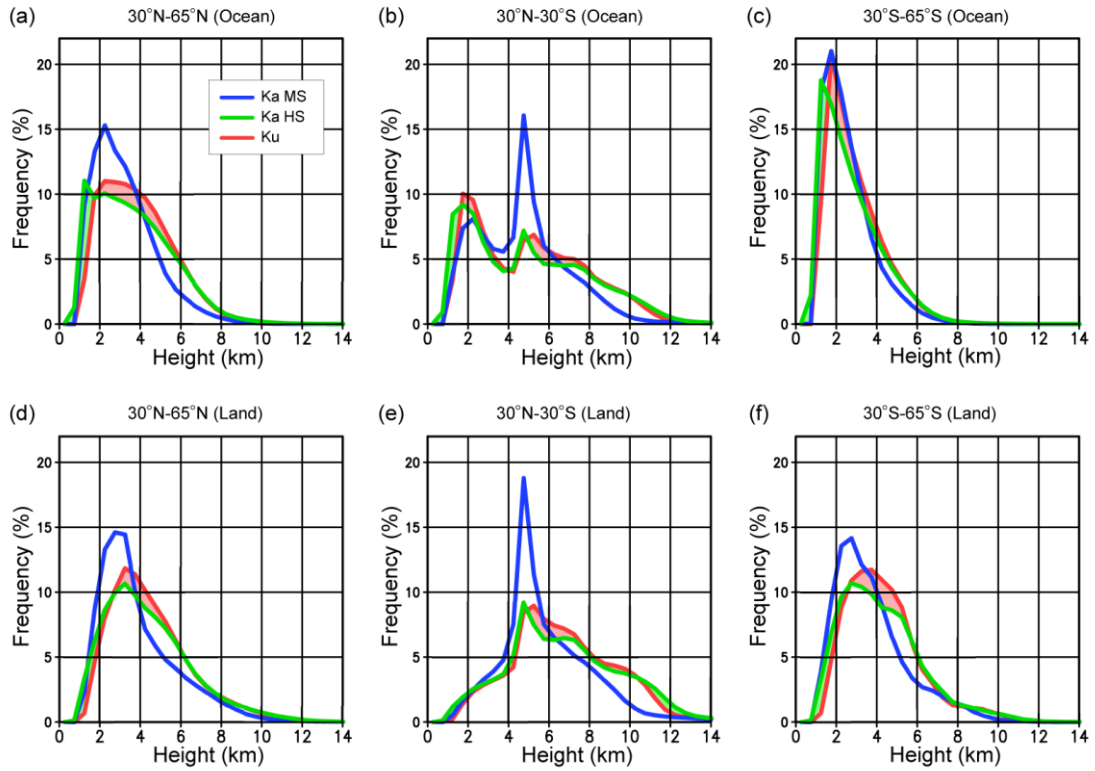


Figure 3-3

The STH histogram for Ku, Ka MS, and Ka HS for (a) 30°N-65°N ocean, (b) 30°S-30°N ocean, (c) 30°S-65°S ocean, (d) 30°N-65°N land, (e) 30°S-30°N land, (f) 30°S-65°S land. For visual clarity, the difference between Ku and Ka HS is shaded in red where Ku exceeds Ka HS and in green otherwise.

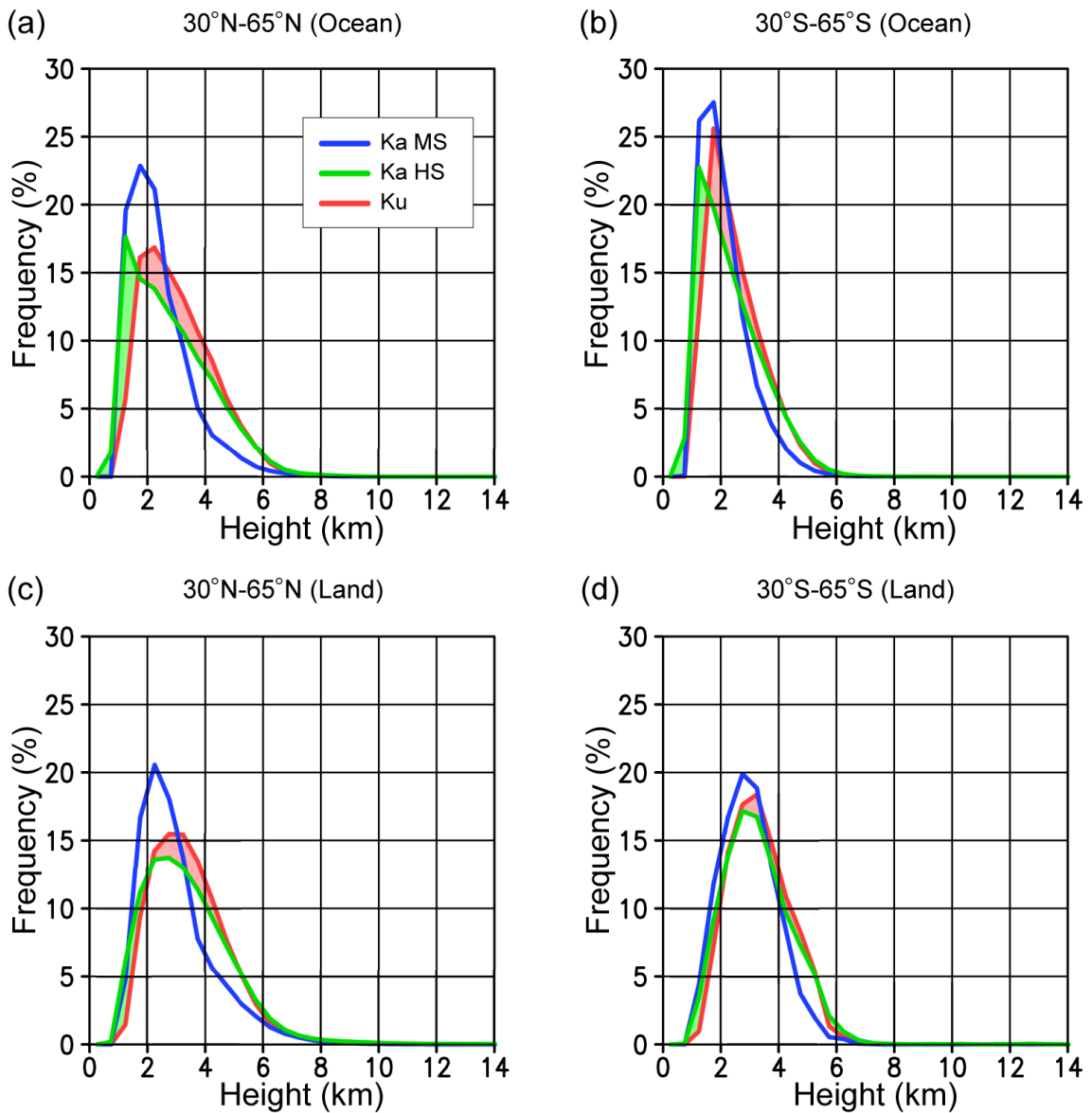


Figure 3-4

As Figure 2a, c, d and f, but only for the regions where surface air temperature at 2 m is

below 0°C. (a) 30°N-65°N ocean, (b) 30°S-65°S ocean, (c) 30°N-65°N land, (d)

30°S-65°S land.

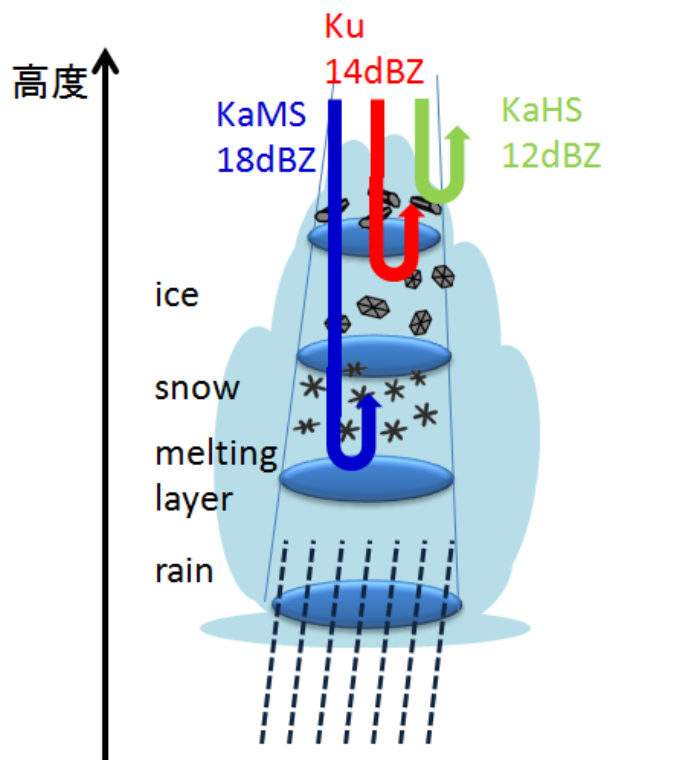


Figure 3-5

The sensitivity for Ka MS is lower than that of Ku and Ka HS, the detection of ice particle in the upper level is missing.

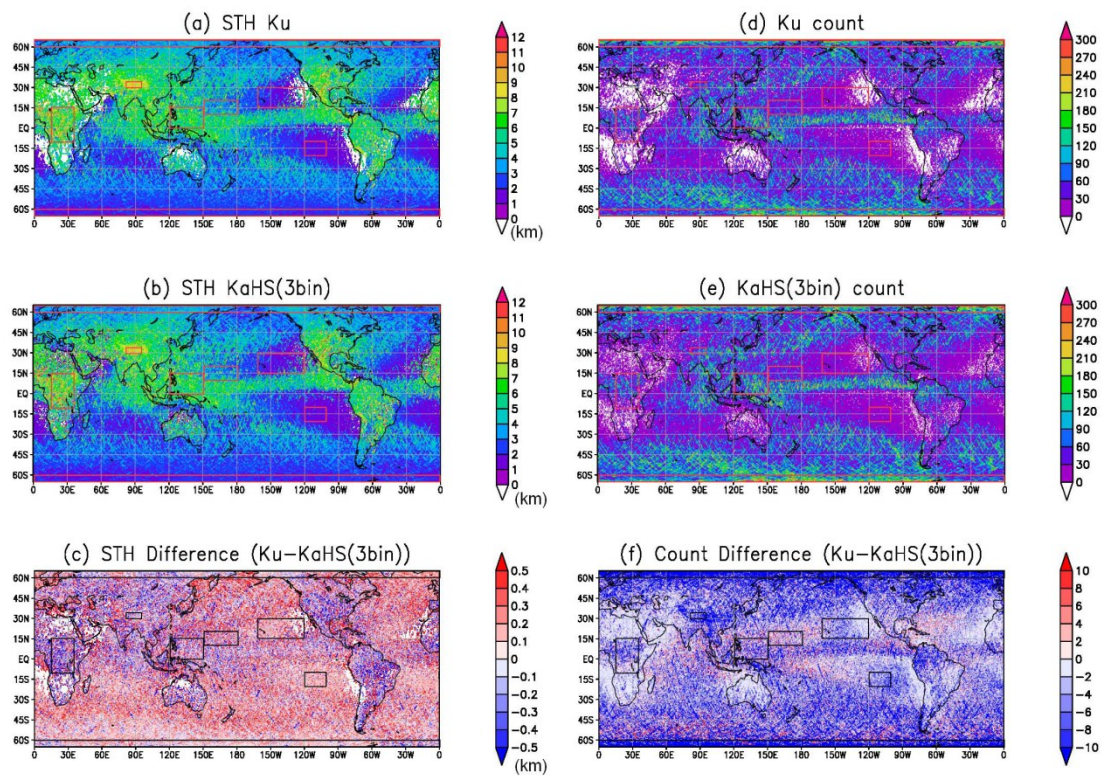


Figure 4-1

Global map of STH and pixel counts for Ku (a and d), KaHS (b and e), and Ku minus Ka HS (c and f). The selected regions are indicated by boxes (Tropical west Pacific, Central Pacific, Northeast Pacific, Southeast Pacific, African rain forest, Tibetan Plateau, North high latitude, South high latitude).

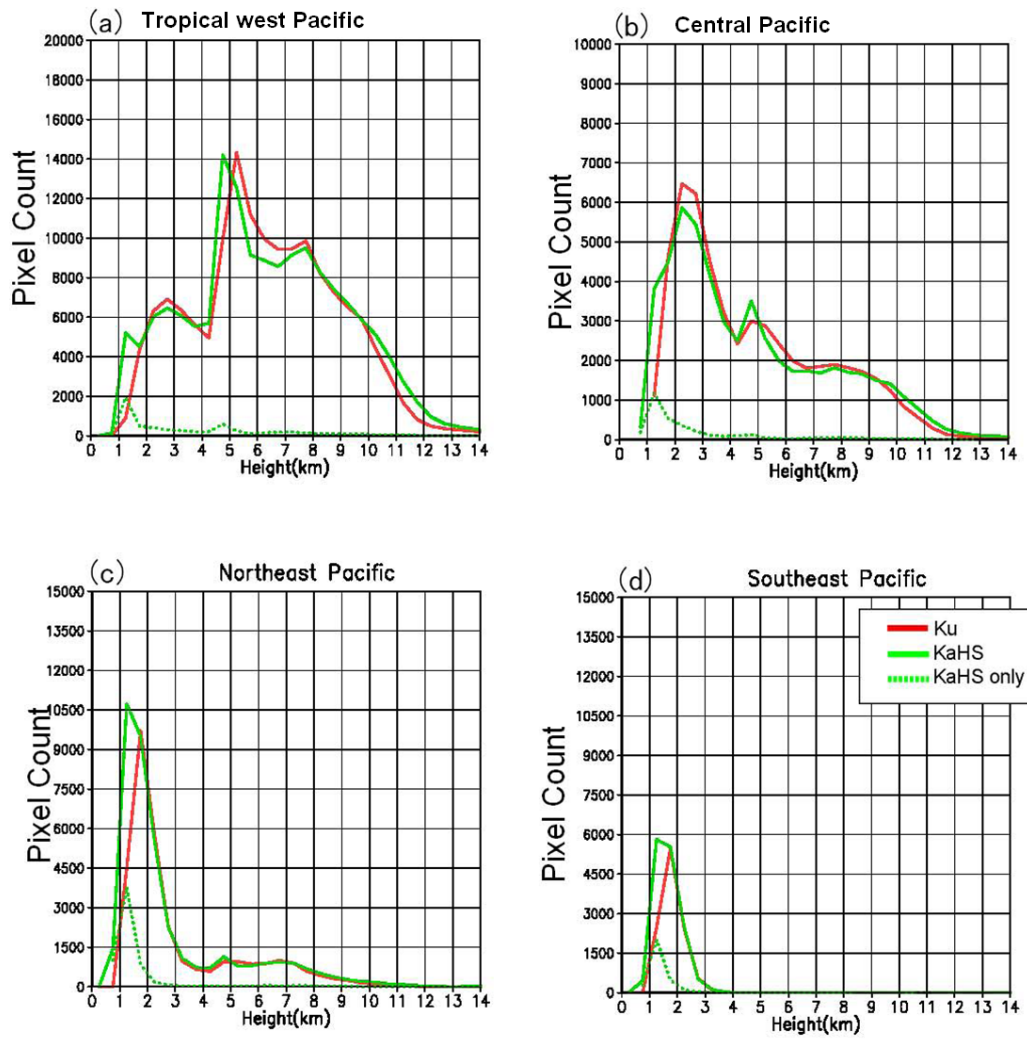


Figure 4-2

The STH histograms for the selected regions (a) Tropical west pacific, (b) Central Pacific, (c) Northeast Pacific, (d) Southeast Pacific.

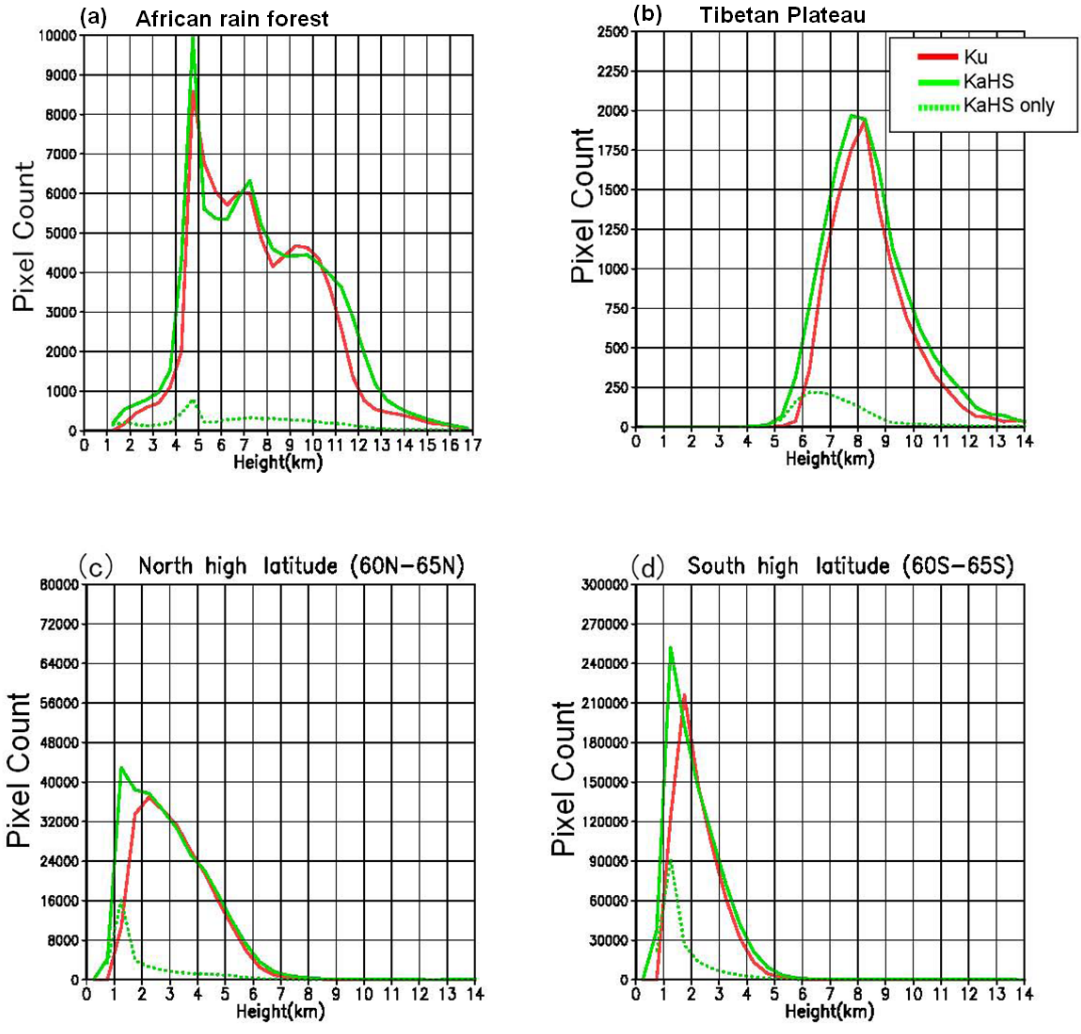
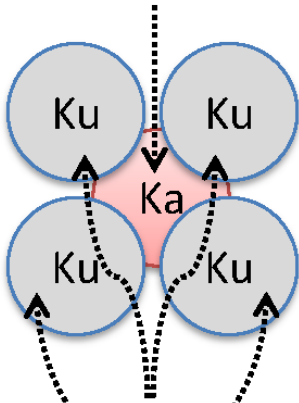


Figure 4-3

As for Figure 2 but (a) African rain forest, (b) Tibetan Plateau, (c) North high latitude, (d) South high latitude.

KaHS only detected

STH detected sample



No detected

Figure 4-4

Schematic for defining pixels with precipitation detected only by Ka HS.

	(%)	
	Ku_{all}/Ka_{all}	Ka_{only}/Ka_{all}
Northwest Pacific	95.4	3.9
Central Pacific	97.9	6.1
Northeast Pacific	80.1	15.9
Southeast Pacific	73.5	19.8
African rain forest	90.0	6.6
Tibetan Plateau	80.9	9.5
North high latitude	82.8	12.7
South high latitude	78.6	20.2

Table 4-1

Number fraction of Ku detected precipitation (Ku_{all} , middle column) and precipitation detected only by Ka HS (Ka_{only} , right column) as normalized by Ka HS detected precipitation (Ka_{all}) for each selected region.

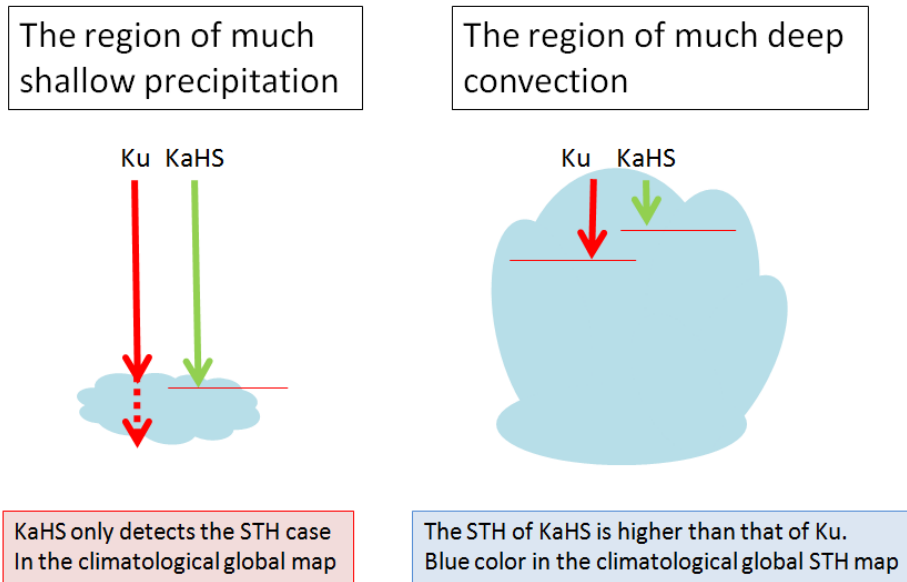


Figure 4-5

Schematic image of summary

KaHS has higher sensitivity for the shallower precipitation than Ku. The STH climatological map shows lower STH in this regime. While much of deep convection in Tropical west Pacific and African rain forest, Ka HS is presumably somewhat better in the ability to detect ice particles aloft in deep convection. The STH difference climatological map shows higher (blue region) STH difference in this regime.